Article

Epitaxial Growth and Electronic Properties of Single- and Few-Layer FeBr$_2$ on Bi(111)

Shigemi Terakawa,* Shinichiro Hatta, Hiroshi Okuyama, and Tetsuya Aruga

ACCESS | Metrics & More | Article Recommendations

ABSTRACT: Magnetic van der Waals (vdW) materials have attracted considerable attention in recent years because of their future spintronics applications. 3d Transition metal dihalides are a promising class of materials to realize two-dimensional vdW magnets with intriguing magnetic and electronic properties. We report the epitaxial growth of (0001)-oriented FeBr$_2$ films from the monolayer by molecular beam epitaxy on the Bi(111) surface. The atomic structure was confirmed to be identical to that of the bulk FeBr$_2$ crystal by dynamical low-energy electron diffraction analysis. Angle-resolved photoelectron spectroscopy revealed that the topmost valence band composed of Fe 3d orbitals is located at 2.2 eV below the Fermi level, showing that the FeBr$_2$ films are insulating down to the monolayer.
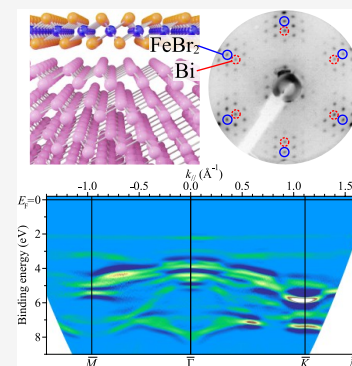
INTRODUCTION

Since the discovery of graphene and its astonishing physical properties,[1,2] two-dimensional (2D) van der Waals (vdW) materials have been attracting extensive attention. Magnetic vdW materials are of particular interest as they are promising for future spintronic applications.[3–9] Furthermore, the vdW magnets can be used to fabricate heterostructures with various materials including topological insulators and superconductors to exploit magnetic proximity effects, which leads to the realization of novel quantum phases such as the topological superconductivity and the quantum anomalous Hall effect.[10–12] Recent experimental studies found ferromagnetic order in atomically thin vdW materials such as CrI$_3$,[13] CrBr$_3$,[14] CrCl$_3$,[15] Cr$_2$Ge$_2$Te$_6$,[16] and Fe$_3$GeTe$_2$.[17] 3d Transition metal dihalides are also good candidates for realizing 2D magnets because many of them have layered structure in bulk and exhibit a rich variety of magnetic states.[18] In theoretical calculations, their monolayers exhibit energetically and dynamically stable magnetic ground states depending on their component metal and halogen atoms. Experimental research of their monolayers has only just begun and their physical properties have been experimentally investigated in only a few transition metal dihalides including FeCl$_2$, NiBr$_2$, and NiI$_2$.[19–23]

FeBr$_2$ has a CdI$_2$-type layered structure, where Br−Fe−Br triple layers (TLs) with hexagonal 1T configuration are stacked along the [0001] axis with weak vdW-type interaction. The monolayer FeBr$_2$ corresponds to the 1-TL film. Bulk FeBr$_2$ is an Ising-type antiferromagnetic insulator with a Néel temperature (T_N) of 14.2 K.[24,25] The magnetic moments on the Fe

atoms are ferromagnetically aligned perpendicular to the (0001) plane in each TL, and they are antiferromagnetically coupled between adjacent TLs. Many theoretical works commonly predict that the in-plane ferromagnetic order remains in the 1-TL film of FeBr$_2$ and isomorphous FeCl$_2$.[26–31] On the other hand, the calculated electronic structures are controversial: some say that they are half-metallic[26–28] and the others say insulating.[30–32] Therefore, it is important to establish a method to fabricate ultrathin FeBr$_2$ films and experimentally reveal the electronic properties. Moreover, it is interesting to investigate the effect of the interaction with the substrate on the physical properties of the films.

In this study, we report the growth of high-quality ultrathin FeBr$_2$ films by molecular beam epitaxy (MBE) on the hexagonal Bi(111) surface. Low-energy electron diffraction (LEED) experiments and dynamical analysis showed that the (0001)-oriented FeBr$_2$ films are epitaxially grown and that the atomic structure is identical to that of bulk FeBr$_2$. The 1-TL film shows sharp satellite spots attributed to a moiré pattern due to lattice matching of FeBr$_2$(0001) to Bi(111) in a ratio of 13:11. Angle-resolved photoelectron spectroscopy (ARPES) measurements revealed that the FeBr$_2$ films have insulating
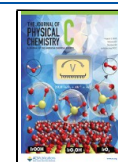
electronic structure down to monolayer with the topmost valence band composed of Fe 3d located at 2.2 eV below the Fermi level. The difference between multilayer and monolayer was found as a significant narrowing of the Br 4p bands, which is attributed to the disappearance of Br−Br interlayer interaction in the monolayer.

METHODS

All experiments were carried out in an ultrahigh vacuum (UHV) chamber with a base pressure of ∼1 × 10^{-10} Torr. Bi(111) substrates were prepared as a single-crystalline film grown on Si(111). Si(111) substrates (n-type) were cleaned by direct-current heating at 1500 K. Bi was deposited on the clean Si(111) (7 × 7) surface at room temperature (RT) at a thickness of 6 nm, and then, the Bi films were annealed at around 400 K to obtain uniform (111)-oriented terraces as reported in the literature.[33,34] FeBr$_2$ powder in a tantalum crucible was heated at 620 K and deposited onto the Bi(111) surface at RT followed by annealing at 490 K for half a minute. The thickness of FeBr$_2$ was measured by a quartz microbalance.

LEED and ARPES measurements were conducted in situ with LEED optics (OCI BDL600) and a hemispherical electron energy analyzer (Scienta R3000), respectively. ARPES data were obtained with monochromatized He Iα and He IIα radiation (hν = 21.2 and 40.8 eV, respectively). The Fermi level was determined from a Fermi edge measured on a tantalum foil in contact with the samples.

Density functional theory (DFT) calculations were performed using the projector-augmented-wave (PAW) method[35,36] implemented in the Vienna Ab initio Simulation Package (VASP).[37−39] The atomic positions were fully optimized using the optB86b-vdW functional,[40] and the band structures were calculated using the spin-polarized Perdew−Burke−Ernzerhof (PBE) functional.[41] The kinetic energy cutoff was set to 475 eV. The Γ-centered 11 × 11 × 1 k-point mesh was used to sample the Brillouin zones (BZs).

RESULTS AND DISCUSSION

Figure 1a shows a LEED pattern of the Bi(111) film. The measured in-plane lattice constant of 4.48 Å agrees with the previously reported value.[33] The threefold LEED pattern reflects the twin-free structure of the Bi film. Sharp spots and low background intensity indicate the high quality of the Bi film. Figure 1b shows a LEED pattern of the FeBr$_2$ film at a thickness of 4.0 TL. The locations of the Bi(111) spots are
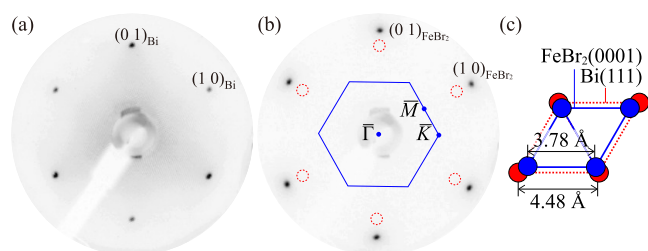
indicated by the red dotted circles in Figure 1b. The six spots of the FeBr$_2$ film are located outside of the Bi(111) spots. The in-plane lattice constant was measured to be 3.78 ± 0.01 Å, which agrees with the lattice constant of the bulk FeBr$_2$(0001) plane (3.776 Å).[42] The corresponding unit cells in real space are displayed in Figure 1c. The LEED patterns show the epitaxial growth of FeBr$_2$(0001) on Bi(111), where the unit vectors of FeBr$_2$(0001) are parallel to those of Bi(111). The sharpness of the FeBr$_2$ spots is comparable to that of the Bi(111) spots. In contrast to the threefold rotational symmetry of the Bi pattern, the pattern of the FeBr$_2$ film exhibits six-fold symmetry irrespective of incident electron energy. Therefore, the FeBr$_2$ film consists of twin domains whose orientations are rotated by 180° with respect to each other.

In order to determine the atomic structure of the FeBr$_2$ film, we performed LEED I−V measurements for the 4.0-TL film. The thickness (2.5 nm) is large enough to neglect the influence of the FeBr$_2$/Bi interface. LEED patterns at 60−500 eV were recorded in increments of 1 eV at 80 K. An image at a high energy of 330 eV is present in the inset of Figure 3a. The I−V curves were normalized by the primary beam current and averaged over the symmetry equivalent beams. The total energy range was 1742 eV. We examined 12 structure models in Figure 2. The models are all possible stacking sequences of
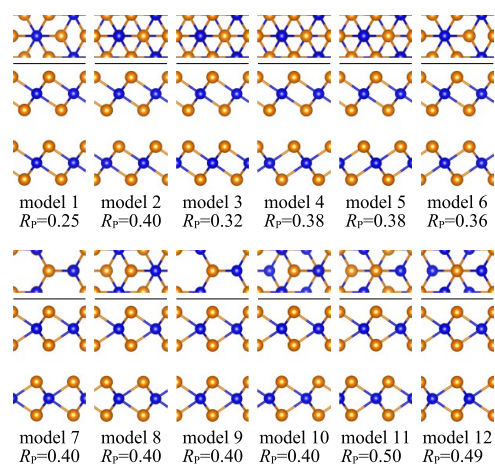

Figure 2. Top and side views of examined structural models and the R_P values for the FeBr$_2$ film. The blue and yellow balls indicate the Fe and Br atoms, respectively. The atomic structures were visualized using VESTA.[43]

TLs with 1T structure for models 1−6 and 1H structure for models 7−12 with threefold rotational symmetry. Model 1 is the CdI$_2$ structure identical to bulk FeBr$_2$. We used the Barbieri−Van Hove symmetrized automated tensor LEED (SATLEED) package for full dynamical calculations[44] and took the coexistence of the twin domains with different orientations into consideration. The calculated and experimental I−V curves were compared by Pendry's reliability factor (R_p).[45] For initial screening, we used phase shifts up to l_{max} = 8, and then, it was increased up to l_{max} = 12 in the further optimization of atomic positions in the topmost six atomic layers (2 TLs). The errors of the structural parameters were evaluated with the Pendry RR function.[45] The calculated R_P values for all of the models are presented in Figure 2. Model 1 shows a notably small R_P value of 0.25 and the variance is 0.04. The other models can be excluded because their R_P values are larger than 0.29.

Figure 1. LEED patterns of the (a) 6-nm Bi(111) film and (b) 4.0-TL FeBr$_2$(0001) film at RT (E_p = 46 eV). The red dotted circles in panel (b) indicate the positions of the Bi(111) spots obtained from panel (a). The blue solid hexagon in panel (b) represents the first Brillouin zone corresponding to FeBr$_2$(0001). (c) The unit cells of FeBr$_2$(0001) (blue solid lines) and Bi(111) (red dotted lines).

We further optimized the structural parameters and Debye temperatures of the best model. The optimum Debye temperatures were 180 K for the topmost Br atoms, 210 K for the Fe atoms, and 260 K for Br atoms beneath. We finally obtained the minimum R_p value of 0.15. The calculated $I-V$ curves (the dotted curves in Figure 3a) are in excellent
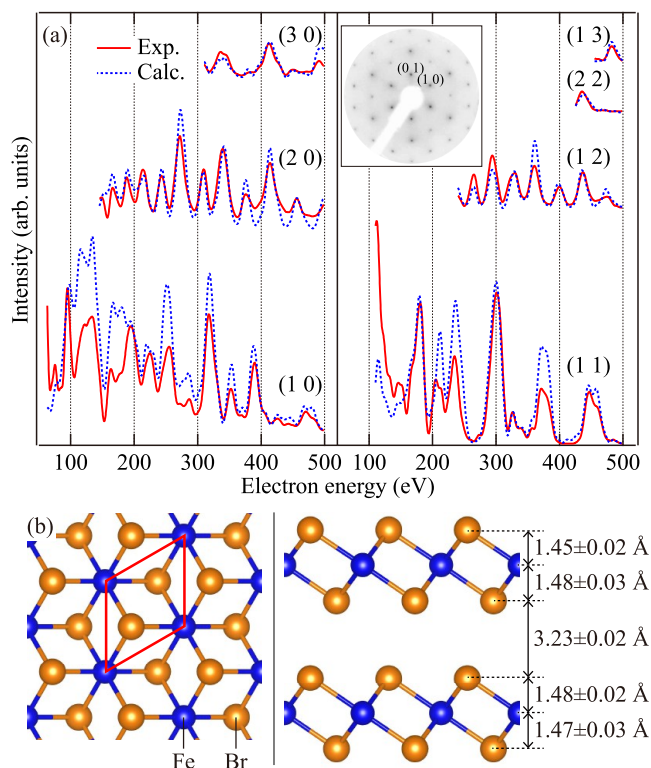

Figure 3. (a) Experimental (solid) and calculated (dotted) LEED $I-V$ curves for the optimized structure. The inset shows the LEED pattern of the 4.0-TL FeBr$_2$ film at 80 K ($E_p = 330$ eV). (b) Top (left) and side (right) views of the optimized FeBr$_2$ structure. The red solid parallelogram represents the unit cell of the FeBr$_2$(0001) plane. The blue and yellow balls indicate the Fe and Br atoms, respectively. The atomic structure was visualized using VESTA.[43]

agreement with the experimental curves (the solid curves). The optimized structure is shown in Figure 3b with the structural

parameters, which agree well with those in the bulk: 1.483 Å for Br−Fe and 3.262 Å for Br−Br.[42]

Figure 4a shows an ARPES band map of the 4.0-TL FeBr$_2$ film at 30 K (see the BZ in Figure 1b). For better identification of band features with a large difference in intensity, the second derivative of energy distribution curves (d^2I/dE^2) is plotted in a color scale shown at the bottom. We found little difference in spectra measured at RT and 30 K except for thermal broadening at RT. The observed valence band structure of FeBr$_2$ is understood by dividing it into two parts above and below 3.7 eV. This is intuitively indicated by a considerable difference in photoelectron intensity between the two regions, as shown in the raw ARPES data (Figure 4b) and its angle-integrated spectrum (the red solid curve in Figure 4d). In the lower region, many bands mainly derived from Br 4p orbitals disperse strongly upward or downward from $\bar{\Gamma}$ and show backfolding according to the BZ of FeBr$_2$(0001). In contrast, the dispersions of the two bands in the upper region are quite weak. Especially, the upper band at 2.2 eV is nearly flat. The small dispersion of the upper two bands indicates that they have large contributions of localized Fe 3d orbitals.

The photoemission cross section for Fe 3d is increased by increasing photon energy from 21.2 eV (He Iα) to 40.8 eV (He IIα).[46] Figure 4b,c presents the ARPES data as plots of photoemission intensity measured with He Iα and He IIα, respectively. Figure 4d shows the comparison of the angle-integrated energy distribution curves with He Iα (red solid curve) and He IIα (blue dotted curve). These spectra were normalized with respect to the maximum intensity. Although the band dispersions measured with the two photon energies generally agree with each other, the two upper bands at 2.2 and 3.2 eV show a drastic increase with He IIα, which supports the above assignment of the two bands as the Fe 3d bands. In addition, the band at around 5 eV at $\bar{K}$ is also enhanced with He IIα, indicating that there are Fe 3d-derived bands as well as Br 4p bands in the lower energy region. It is noted that there is no state at the Fermi level even in the integrated spectra both with He Iα and He IIα. This shows that the 4.0-TL film is insulating, and the valence band maximum is located at 2.2 eV below the Fermi level.

The above results indicate that the electronic properties of the FeBr$_2$(0001) film at a thickness of 4.0 TL (2.5 nm) are consistent with the insulating nature of bulk FeBr$_2$. It is more
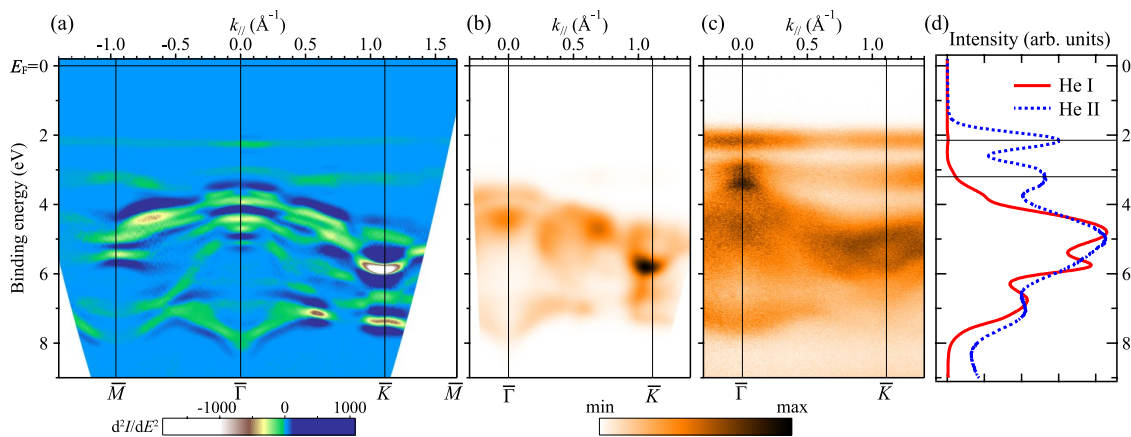

Figure 4. (a) Second derivative of the ARPES band map of the 4.0-TL FeBr$_2$ film at 30 K along $\bar{M}-\bar{\Gamma}-\bar{K}-\bar{M}$ measured with He Iα. ARPES band maps of the 4.0-TL FeBr$_2$ film at RT along $\bar{\Gamma}-\bar{K}$ measured with (b) He Iα ($h\nu = 21.2$ eV) and (c) He IIα ($h\nu = 40.8$ eV). (d) Angle-integrated photoelectron spectra of panel (b) red solid curve and panel (c) blue dotted curve.
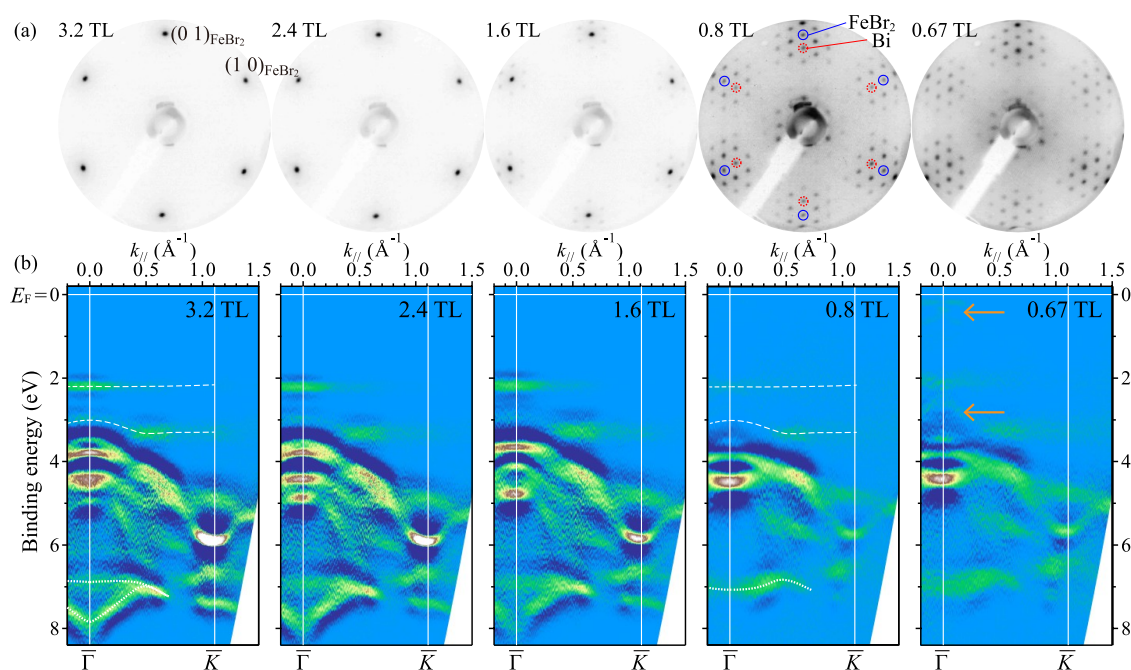
Figure 5. Thickness dependence of the (a) LEED patterns and (b) ARPES band maps along $\overline{\Gamma}-\overline{K}$ of the $FeBr_2$ films with thicknesses of 3.2, 2.4, 1.6, 0.8, and 0.67 TL measured at RT. The red dotted and blue solid circles in the 0.8-TL pattern indicate the spots corresponding to Bi(111) and $FeBr_2(0001)$, respectively. The ARPES data were obtained using He Iα. The arrows on the band map at 0.67 TL indicate the bands from the Bi(111) substrate.

interesting to investigate whether the film thickness can decrease down to a single TL while maintaining crystal quality and how the electronic structure changes with the thickness. In LEED patterns for thinner films, the influence of the $FeBr_2$/Bi interface was found below 2 TL. Figure 5a shows the LEED patterns of the $FeBr_2$ films with thicknesses of 3.2, 2.4, 1.6, 0.8, and 0.67 TL. Thickness-dependent change in the positions of the $FeBr_2$ spots was within the error of the measurement (0.01 $Å^{-1}$). With decreasing thickness, satellite spots surrounding each of the $FeBr_2(0001)$ spots appeared and became intense. The intensity of the satellite spots was maximized at 0.8 TL. The positions of the satellite spots just inside the $FeBr_2(0001)$ spots, which are indicated by the red dotted circles in Figure 5a, were found to coincide with those of the Bi(111) spots (Figure 1a). These spots are sharp even at 1 TL, indicating that the domain size of the $FeBr_2$ film is significantly larger than the electron coherence length of typically 150 Å.

Here we focus on the origin of the multiple satellite spots. We measured the distances between adjacent Bi(111) (1 × 1) spots (the red dotted circles) and $FeBr_2(0001)$ (1 × 1) spots (the blue solid circles) for the 0.8-TL LEED pattern (Figure 5a). The average distance was 0.29 ± 0.01 $Å^{-1}$ and the ratios to the length of the unit reciprocal vectors corresponding to $FeBr_2(0001)$ and Bi(111) were 6.5 and 5.5, respectively. Therefore, the observed complex pattern is not attributed to a hexagonal superlattice described with integer coefficients with respect to the unit vectors of $FeBr_2(0001)$ and Bi(111). Nevertheless, the values of 6.5 and 5.5 suggest the lattice coincidence between $13 \times a_{FeBr_2}$ and $11 \times a_{Bi}$. The in-plane lattice constants of $a_{FeBr_2} = 3.78$ Å and $a_{Bi} = 4.48$ Å show only a small mismatch of 0.3%. The integer difference of 2 between the coefficients 13 and 11 yields a configuration change as "in-phase → out-of-phase → quasi-in-phase → out-of-phase → in-phase" along on the lines parallel to unit vectors as shown in

the schematic model of Figure 6. As the in-phase and quasi-in-phase configurations modulate atomic positions in a similar
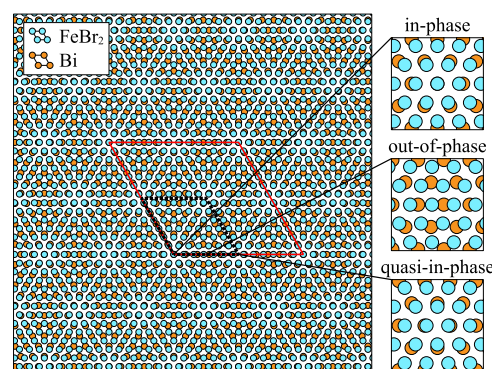

Figure 6. Schematic model of the $FeBr_2(0001)$ and Bi(111) lattices when assuming the commensurate structure of $(13 \times 13)_{FeBr_2} = (11 \times 11)_{Bi}$. The blue and orange circles represent the lattice points of $FeBr_2(0001)$ and Bi(111), respectively. The red solid and black dotted parallelograms represent the superlattice of $(13 \times 13)_{FeBr_2} = (11 \times 11)_{Bi}$ and the quasi-superlattice of $(6.5 \times 6.5)_{FeBr_2} = (5.5 \times 5.5)_{Bi}$, respectively. The in-phase, out-of-phase, and quasi-in-phase configurations are enlarged on the right.

way, the diffraction pattern should be characterized by the half period of $13 \times a_{FeBr_2}$, namely, 6.5 with respect to $FeBr_2(0001)$, and likewise, 5.5 with respect to Bi(111), indicated by the black dotted parallelogram in Figure 6. These values are consistent with the LEED observation. Such modulation is expected to be observed by scanning tunneling microscopy (STM) as a moiré pattern. Note that it is still unknown whether the small mismatch of 0.3% causes relaxation in the Bi(111) or 1-TL $FeBr_2$ structure although the LEED pattern
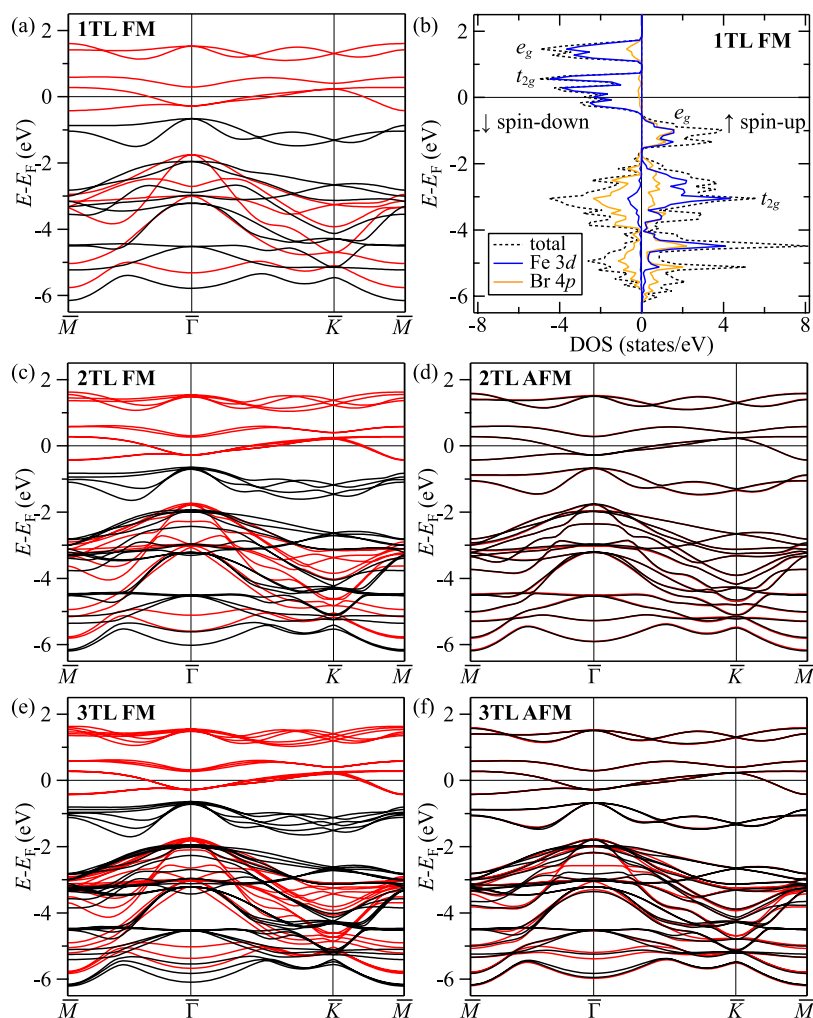
Figure 7. Calculated band structures of $FeBr_2$ with different thicknesses and magnetic states: (a) 1-TL FM, (c) 2-TL FM, (d) 2-TL AFM, (e) 3-TL FM, and (f) 3-TL AFM. The black and red lines represent the spin-up and spin-down channels, respectively. (b) Calculated total DOS (the black dashed lines) and partial DOS (the blue and orange solid lines) of 1-TL $FeBr_2$ with FM state.

suggests a commensurate superstructure of $(13 \times 13)_{FeBr_2} = (11 \times 11)_{Bi}$. This is because the lattice relaxation of 0.3% ($\sim$0.01 Å) is within the uncertainty of the LEED measurement.

Figure 5b shows ARPES band maps of the $FeBr_2$ films for the same thicknesses set in panel (a). We first describe the band structure change from 3.2 to 0.8 TL. For the Br 4p bands, thickness-dependent changes were clearly found near $\bar{\Gamma}$; the top part of the Br band was gradually flattened and shifted downward from 3.2 to 0.8 TL, and the bottom part showed the disappearance of the lowest band at around 8 eV from 1.6 to 0.8 TL as indicated by the white dotted curves. The remarkable narrowing of the Br bandwidth from multilayer to monolayer is related to the disappearance of the Br–Br electronic interaction between adjacent TLs. In contrast, thickness-dependent change was negligible for the two Fe 3d bands indicated by the white dashed curves. Furthermore, no new feature was observed near the Fermi level, showing that the 1-TL $FeBr_2$ film is insulating as well as the thicker films.

When the thickness was decreased below 0.8 TL, new band features were seen near $\bar{\Gamma}$ at 0.0–0.9 and 2.2–3.1 eV as indicated by the orange arrows in the 0.67-TL band map in Figure 5b. These bands correspond to the ones from the Bi(111) substrate. Except for the Bi bands, no change was observed between the 0.8-TL and 0.67-TL films. The stronger

Bi(111) band features below 0.8 TL and the highest intensity of the LEED satellite spots at 0.8 TL suggest that the monolayer is completed at the 0.8-TL thickness and that the thickness is slightly underestimated. Considering that the deposition rate was determined by the thickness measured in a thick-film regime of $FeBr_2$ with a quartz microbalance, the underestimation might be attributed to a higher sticking probability of $FeBr_2$ on Bi compared to $FeBr_2$ on $FeBr_2$. The overall band feature of $FeBr_2$ at 0.8–3.2 TL was as sharp as the 4.0-TL film. The sharp moiré LEED pattern and ARPES band structure indicate successful growth of the epitaxial $FeBr_2$ films from the monolayer. Nevertheless, the observed band structure did not show distinct thickness dependence such as the increase of the number of valence bands with the number of TL. Thus, layer-by-layer growth on multi-TL films has not been confirmed and real-space measurements using, for example, STM is required.

In order to gain more insight into the magnetic and electronic properties of the ultrathin $FeBr_2$ films, we performed first-principles total energy and band structure calculations for free-standing $FeBr_2$ films with thicknesses of 1, 2, and 3 TL. Previous theoretical works predict that 1-TL $FeBr_2$ has a ferromagnetic (FM) order with the high-spin d^6 configuration of the Fe^{2+} ion.[27,30] Here, we examined the interlayer magnetic

couplings. We compared the total energies of 2 TL, 3 TL, and bulk FeBr$_2$ with FM and antiferromagnetic (AFM) interlayer couplings while preserving the intralayer FM coupling and found that the AFM coupling is more favorable than the FM coupling for all of the structures. The total energy differences between the AFM and FM states per TL−TL interface were calculated to be −15.0, −8.2, and −9.4 meV for 2 TL, 3 TL, and bulk FeBr$_2$, respectively. The result suggests that the AFM stacking of the bulk FeBr$_2$ persists down to 2 TL with almost the same or even higher transition temperature. The calculated magnetic moments per unit cell are 4.16μ_B in all of the FeBr$_2$ structures, which are in good agreement with the experimental value of 4.4μ_B for bulk FeBr$_2$.[24]

We next calculated the band structure for 1 TL, 2 TL, and 3 TL FeBr$_2$ with FM and AFM configurations. Figure 7a,b shows the spin-resolved band structure and density of states (DOS) of 1-TL FeBr$_2$ in the FM state, respectively. The valence bands are mainly composed of Fe 3d and Br 4p orbitals. The partial DOS for Fe 3d and Br 4p shows a good agreement with that previously calculated for bulk FeBr$_2$.[47] The Fe 3d orbitals are split into two higher-lying e$_g$ states and three lower-lying t$_{2g}$ states by the octahedral crystal field formed by the six neighboring Br atoms. For the spin-down channel (the red lines in Figure 7a and the left part of Figure 7b), the Fe 3d and Br 4p bands are energetically separated. The Br 4p orbitals form highly dispersive bands below the Fermi level and the Fe 3d e$_g$ and t$_{2g}$ orbitals form unoccupied and partially occupied weakly dispersive bands, respectively. The Fe 3d states in the spin-up channel (the black lines in Figure 7a and the right part of Figure 7b) are fully occupied and located in the same energy range as the Br 4p states. The e$_g$ bands are located at around −1 eV and the t$_{2g}$ bands are not clearly distinguishable from the dispersive Br 4p bands. The Fe 3d and Br 4p contributions to the band structures of 2-TL and 3-TL FeBr$_2$ can be understood in the same way.

We compare the calculated band structures with the experimental ones. Although the measurement temperature is higher than the bulk magnetic transition temperature of 14.2 K,[24,25] at which the magnetic long-range order disappears, the short-range order still exists with a finite correlation length and the measured states are considered to be close to the mixing states between the interlayer AFM and FM states. Indeed, the band structures calculated for the FM or AFM states agree much better with the experimental ones than those calculated for the nonmagnetic states. Such agreement between band structures calculated for FM states and experimental ones above magnetic transition temperatures is also reported for bulk vdW ferromagnets such as VI$_3$, CrI$_3$, and Cr$_2$Ge$_2$Te$_6$.[48−50]

Thickness-dependent change of the band structures is mainly found on the bottom bands located in the energy range of −5 to −6 eV at $\bar{\Gamma}$. These bands are composed of Br 4p$_z$ orbitals pointing in the out-of-plane direction and are significantly affected by the TL−TL interface. This is consistent with the experimental result that the pronounced change from monolayer to multilayer is observed in the bottom bands at $\bar{\Gamma}$. For monolayer FeBr$_2$, the band is observed as a single band (see the 0.8-TL panel of Figure 5b), while there are two spin-splitted bands in the calculation. This discrepancy can be understood by considering that our measurement temperature is higher than the magnetic transition temperature and that the width of the observed band itself (0.5 eV) is comparable to the calculated splitting of 0.47 eV. For thicker FeBr$_2$, the bands are observed as two bands separated by 0.9

eV (see the white dotted lines in the left panel of Figure 5b). In the calculation for the FM states, the bandwidth increases to 0.91 eV (2 TL) and 1.07 eV (3 TL) because of the formation of new states by the hybridization between the states on different TLs with each spin orientation. On the other hand, in the calculation for the AFM states, the spin on each TL has an opposite direction and thus the hybridization between the states on different TLs is much weaker. As a result, the number of almost energetically degenerate bands is increased with two center energies at −5 and −6 eV, and the bandwidth changes to 0.64 eV (2 TL) and 0.78 eV (3 TL). The calculation for the AFM states reproduces the experimental observation showing two separate bands regardless of TL number, while the values of the bandwidth calculated for the FM states are closer to the experimental ones. It should also be noted that the downward shift and flattening of the upper Br 4p bands observed by ARPES are not reproduced by our calculation, implying the influence of the Bi(111) surface in the thinner films.

Finally, we describe the Fe 3d bands involved in the magnetic properties of FeBr$_2$. In some theoretical studies[26−28] as well as our calculations, the Fe 3d band of FeBr$_2$ is predicted to be metallic. In our ARPES measurements, the topmost Fe 3d band was observed at 2.2 eV below the Fermi level down to the monolayer. Compared to the ARPES results in Figures 4 and 5 with the calculated band structures in Figure 7, it is reasonable to assign the flat band at 2.2 eV to the partially occupied t$_{2g}$ bands and the slightly dispersive band at 3 eV to the occupied e$_g$ bands although the experimental binding energies disagree with those in the calculations. This assignment is also consistent with the experimental result that the 2.2-eV band shows a greater increase in intensity than the 3-eV band in the measurement with He Iα and He IIα, indicating that the 2.2-eV band has a larger Fe 3d contribution. The discrepancy between the experimental and calculated band structures suggests the difficulty in the theoretical prediction of the electronic properties of the FeBr$_2$ film. As mentioned in the previous theoretical work,[30,32] the structural parameters, electron correlation, and spin−orbit interaction strongly affect the calculated electronic structure. These parameters not only influence the Fe 3d bands but also affect Br 4p bands.[29] The energy relationship of the lowest bands at $\bar{M}$ and $\bar{K}$ is calculated to be reversed depending on the electron correlation value. The lowest band at $\bar{M}$ is experimentally observed at higher binding energy than that at $\bar{K}$. In addition, the calculated width of the Fe 3d band is typically more than 0.5 eV, which is not consistent with the experimentally observed nearly flat band. Future theoretical work is required to quantitatively evaluate these parameters and further understand the electronic structure and interaction between the magnetic and electronic properties of the promising vdW magnet, FeBr$_2$.

■ CONCLUSIONS

In summary, we have demonstrated the MBE growth of few-layer (0001)-oriented FeBr$_2$ films on the Bi(111) surface by LEED and ARPES. The sharp LEED pattern with multiple moiré spots and the clear distinction in band structure between the multilayer and monolayer films indicate that the FeBr$_2$ film is epitaxially grown from the monolayer. The electronic structure of the films is insulating down to the monolayer, where the topmost Fe 3d band is located at 2.2 eV below the Fermi level. The establishment of the high-quality ultrathin FeBr$_2$ films on Bi(111) with a sharp moiré pattern will

encourage further investigation not only on the magnetic properties of the few-layer $FeBr_2$ films but also on the physical properties of the interface between the magnetic layers and the Bi(111) surface with spin-polarized metallic states due to strong Rashba-type spin−orbit interaction.[51]

■ AUTHOR INFORMATION

Corresponding Author

   Shigemi Terakawa − *Nano-Systems from Ions, Spins and Electrons, Max Planck Institute of Microstructure Physics, Halle 06120, Germany; Department of Chemistry, Graduate School of Science, Kyoto University, Kyoto 606-8502, Japan;* ⊙ orcid.org/0000-0001-5790-7234; Email: sterakawa@mpi-halle.mpg.de

Authors

   Shinichiro Hatta − *Department of Chemistry, Graduate School of Science, Kyoto University, Kyoto 606-8502, Japan;* ⊙ orcid.org/0000-0001-5034-5187

   Hiroshi Okuyama − *Department of Chemistry, Graduate School of Science, Kyoto University, Kyoto 606-8502, Japan;* ⊙ orcid.org/0000-0002-6031-0612

   Tetsuya Aruga − *Department of Chemistry, Graduate School of Science, Kyoto University, Kyoto 606-8502, Japan*

Complete contact information is available at:
https://pubs.acs.org/10.1021/acs.jpcc.3c02188

■ REFERENCES

(1) Geim, A. K.; Novoselov, K. S. The rise of graphene. *Nat. Mater.* **2007**, *6*, 183−191.

(2) Castro Neto, A. H.; Guinea, F.; Peres, N. M. R.; Novoselov, K. S.; Geim, A. K. The electronic properties of graphene. *Rev. Mod. Phys.* **2009**, *81*, 109−162.

(3) Burch, K. S.; Mandrus, D.; Park, J.-G. Magnetism in two-dimensional van der Waals materials. *Nature* **2018**, *563*, 47−52.

(4) Gong, C.; Zhang, X. Two-dimensional magnetic crystals and emergent heterostructure devices. *Science* **2019**, *363*, No. 706.

(5) Li, H.; Ruan, S.; Zeng, Y.-J. Intrinsic van der Waals magnetic materials from bulk to the 2D limit: new frontiers of spintronics. *Adv. Mater.* **2019**, *31*, No. 1900065.

(6) Wang, M. C.; Huang, C. C.; Cheung, C. H.; Chen, C. Y.; Tan, S. G.; Huang, T. W.; Zhao, Y.; Zhao, Y.; Wu, G.; Feng, Y. P.; et al. Prospects and opportunities of 2D van der Waals magnetic systems. *Ann. Phys.* **2020**, *532*, No. 1900452.

(7) Cortie, D. L.; Causer, G. L.; Rule, K. C.; Fritzsche, H.; Kreuzpaintner, W.; Klose, F. Two-dimensional magnets: forgotten history and recent progress towards spintronic applications. *Adv. Funct. Mater.* **2020**, *30*, No. 1901414.

(8) Blei, M.; Lado, J. L.; Song, Q.; Dey, D.; Erten, O.; Pardo, V.; Comin, R.; Tongay, S.; Botana, A. S. Synthesis, engineering, and theory of 2D van der Waals magnets. *Appl. Phys. Rev.* **2021**, *8*, No. 021301.

(9) Wang, Q. H.; Bedoya-Pinto, A.; Blei, M.; Dismukes, A. H.; Hamo, A.; Jenkins, S.; Koperski, M.; Liu, Y.; Sun, Q.-C.; Telford, E. J.; et al. The magnetic genome of two-dimensional van der Waals materials. *ACS Nano* **2022**, *16*, 6960−7079.

(10) Bora, M.; Deb, P. Magnetic proximity effect in two-dimensional van der Waals heterostructure. *J. Phys. Mater.* **2021**, *4*, No. 034014.

(11) Tokura, Y.; Yasuda, K.; Tsukazaki, A. Magnetic topological insulators. *Nat. Rev. Phys.* **2019**, *1*, 126−143.

(12) Kezilebieke, S.; Huda, M. N.; Vaňo, V.; Aapro, M.; Ganguli, S. C.; Silveira, O. J.; Głodzik, S.; Foster, A. S.; Ojanen, T.; Liljeroth, P. Topological superconductivity in a van der Waals heterostructure. *Nature* **2020**, *588*, 424−428.

(13) Huang, B.; Clark, G.; Navarro-Moratalla, E.; Klein, D. R.; Cheng, R.; Seyler, K. L.; Zhong, D.; Schmidgall, E.; McGuire, M. A.; Cobden, D. H.; et al. Layer-dependent ferromagnetism in a van der Waals crystal down to the monolayer limit. *Nature* **2017**, *546*, 270−273.

(14) Kim, M.; Kumaravadivel, P.; Birkbeck, J.; Kuang, W.; Xu, S. G.; Hopkinson, D. G.; Knolle, J.; McClarty, P. A.; Berdyugin, A. I.; Shalom, M. B.; et al. Micromagnetometry of two-dimensional ferromagnets. *Nat. Electron.* **2019**, *2*, 457−463.

(15) Bedoya-Pinto, A.; Ji, J. R.; Pandeya, A. K.; Gargiani, P.; Valvidares, M.; Sessi, P.; Taylor, J. M.; Radu, F.; Chang, K.; Parkin, S. S. Intrinsic 2D-XY ferromagnetism in a van der Waals monolayer. *Science* **2021**, *374*, 616−620.

(16) Gong, C.; Li, L.; Li, Z.; Ji, H.; Stern, A.; Xia, Y.; Cao, T.; Bao, W.; Wang, C.; Wang, Y.; et al. Discovery of intrinsic ferromagnetism in two-dimensional van der Waals crystals. *Nature* **2017**, *546*, 265−269.

(17) Fei, Z.; Huang, B.; Malinowski, P.; Wang, W.; Song, T.; Sanchez, J.; Yao, W.; Xiao, D.; Zhu, X.; May, A. F.; et al. Two-dimensional itinerant ferromagnetism in atomically thin Fe_3GeTe_2. *Nat. Mater.* **2018**, *17*, 778−782.

(18) McGuire, M. A. Crystal and magnetic structures in layered, transition metal dihalides and trihalides. *Crystals* **2017**, *7*, 121.

(19) Zhou, X.; Brzostowski, B.; Durajski, A.; Liu, M.; Xiang, J.; Jiang, T.; Wang, Z.; Chen, S.; Li, P.; Zhong, Z.; et al. Atomically thin 1T-$FeCl_2$ grown by molecular-beam epitaxy. *J. Phys. Chem. C* **2020**, *124*, 9416−9423.

(20) Cai, S.; Yang, F.; Gao, C. $FeCl_2$ monolayer on HOPG: Art of growth and momentum filtering effect. *Nanoscale* **2020**, *12*, 16041−16045.

(21) Jiang, S.; Wang, G.; Deng, H.; Liu, K.; Yang, Q.; Zhao, E.; Zhu, L.; Guo, W.; Yang, J.; Zhang, C.; et al. General synthesis of 2D magnetic transition metal dihalides via trihalide reduction. *ACS Nano* **2023**, *17*, 363−371.

(22) Liu, H.; Wang, X.; Wu, J.; Chen, Y.; Wan, J.; Wen, R.; Yang, J.; Liu, Y.; Song, Z.; Xie, L. Vapor deposition of magnetic van der Waals NiI_2 crystals. *ACS Nano* **2020**, *14*, 10544−10551.

(23) Bikaljević, D.; González-Orellana, C.; Peña-Díaz, M.; Steiner, D.; Dreiser, J.; Gargiani, P.; Foerster, M.; Ángel Niño, M.; Aballe, L.; Ruiz-Gomez, S.; et al. Noncollinear magnetic order in two-dimensional $NiBr_2$ films grown on Au(111). *ACS Nano* **2021**, *15*, 14985−14995.

(24) Wilkinson, M. K.; Cable, J. W.; Wollan, E. O.; Koehler, W. C. Neutron diffraction investigations of the magnetic ordering in $FeBr_2$, $CoBr_2$, $FeCl_2$, and $CoCl_2$. *Phys. Rev.* **1959**, *113*, 497−507.

(25) Fert, A. R.; Carrara, P.; Lanusse, M. C.; Mischler, G.; Redoules, J. P. Transition de phase metamagnetique du bromure ferreux. *J. Phys, Chem. Solids* **1973**, *34*, 223−230.

(26) Torun, E.; Sahin, H.; Singh, S. K.; Peeters, F. M. Stable half-metallic monolayers of $FeCl_2$. *Appl. Phys. Lett.* **2015**, *106*, No. 192404.

(27) Ashton, M.; Gluhovic, D.; Sinnott, S. B.; Guo, J.; Stewart, D. A.; Hennig, R. G. Two-dimensional intrinsic half-metals with large spin gaps. *Nano Lett.* **2017**, *17*, 5251−5257.

(28) Feng, Y.; Wu, X.; Han, J.; Gao, G. Robust half-metallicities and perfect spin transport properties in 2D transition metal dichlorides. *J. Mater. Chem. C* **2018**, *6*, 4087−4094.

(29) Kovaleva, E. A.; Melchakova, I.; Mikhaleva, N. S.; Tomilin, F. N.; Ovchinnikov, S. G.; Baek, W.; Pomogaev, V. A.; Avramov, P.; Kuzubov, A. A. The role of strong electron correlations in determination of band structure and charge distribution of transition metal dihalide monolayers. *J. Phys. Chem. Solids* **2019**, *134*, 324−332.

(30) Botana, A. S.; Norman, M. R. Electronic structure and magnetism of transition metal dihalides: Bulk to monolayer. *Phys. Rev. Mater.* **2019**, *3*, No. 044001.

(31) Lu, D.; Liu, L.; Ma, Y.; Yang, K.; Wu, H. A unique electronic state in a ferromagnetic semiconductor $FeCl_2$ monolayer. *J. Mater. Chem. C* **2022**, *10*, 8009−8014.

(32) Yao, Q.; Li, J.; Liu, Q. Fragile symmetry-protected half metallicity in two-dimensional van der Waals magnets: A case study of monolayer $FeCl_2$. *Phys. Rev. B* **2021**, *104*, No. 035108.

(33) Nagao, T.; Sadowski, J. T.; Saito, M.; Yaginuma, S.; Fujikawa, Y.; Kogure, T.; Ohno, T.; Hasegawa, Y.; Hasegawa, S.; Sakurai, T. Nanofilm allotrope and phase transformation of ultrathin Bi film on Si(111)-7×7. *Phys. Rev. Lett.* **2004**, *93*, No. 105501.

(34) Yaginuma, S.; Nagao, T.; Sadowski, J. T.; Pucci, A.; Fujikawa, Y.; Sakurai, T. Surface pre-melting and surface flattening of Bi nanofilms on Si(1 1 1)-7 × 7. *Surf. Sci.* **2003**, *547*, L877−L881.

(35) Blöchl, P. E. Projector augmented-wave method. *Phys. Rev. B* **1994**, *50*, No. 17953.

(36) Kresse, G.; Joubert, D. From ultrasoft pseudopotentials to the projector augmented-wave method. *Phys. Rev. B* **1999**, *59*, No. 1758.

(37) Kresse, G.; Hafner, J. *Ab initio* molecular dynamics for liquid metals. *Phys. Rev. B* **1993**, *47*, No. 558(R).

(38) Kresse, G.; Furthmüller, J. Efficient iterative schemes for *ab initio* total-energy calculations using a plane-wave basis set. *Phys. Rev. B* **1996**, *54*, No. 11169.

(39) Kresse, G.; Furthmüller, J. Efficiency of ab-initio total energy calculations for metals and semiconductors using a plane-wave basis set. *Comput. Mater. Sci.* **1996**, *6*, 15−50.

(40) Klimeš, J.; Bowler, D. R.; Michaelides, A. Van der Waals density functionals applied to solids. *Phys. Rev. B* **2011**, *83*, No. 195131.

(41) Perdew, J. P.; Burke, K.; Ernzerhof, M. Generalized gradient approximation made simple. *Phys. Rev. Lett.* **1996**, *77*, No. 3865.

(42) Haberecht, J.; Borrmann, H.; Kniep, R. Refinement of the crystal structure of iron dibromide, $FeBr_2$. *Z. Kristallogr. - New Cryst. Struct.* **2001**, *216*, 510.

(43) Momma, K.; Izumi, F. VESTA 3 for three-dimensional visualization of crystal, volumetric and morphology data. *J. Appl. Crystallogr.* **2011**, *44*, 1272−1276.

(44) Barbieri, A.; Hove, M. A. V. *Symmetrized Automated Tensor Leed (SATLEED) package available from M. A. Van Hove*.

(45) Pendry, J. B. Reliability factors for LEED calculations. *J. Phys. C: Solid State Phys.* **1980**, *13*, 937−944.

(46) Yeh, J. J.; Lindau, I. Atomic subshell photoionization cross sections and asymmetry parameters: $1 \leq Z \leq 103$. *At. Data Nucl. Data Tables* **1985**, *32*, 1−155.

(47) Rusz, J.; Sargolzaei, M. Spin and orbital magnetism of $FeBr_2$: a density functional theory study. *J. Phys.: Condens. Matter* **2008**, *20*, No. 025217.

(48) Kundu, A. K.; Liu, Y.; Petrovic, C.; Valla, T. Valence band electronic structure of the van der Waals ferromagnetic insulators: VI_3 and CrI_3. *Sci. Rep.* **2020**, *10*, No. 15602.

(49) De Vita, A.; Nguyen, T. T. P.; Sant, R.; Pierantozzi, G. M.; Amoroso, D.; Bigi, C.; Polewczyk, V.; Vinai, G.; Nguyen, L. T.; Kong, T.; et al. Influence of orbital character on the ground state electronic properties in the van der Waals transition metal iodides VI_3 and CrI_3. *Nano Lett.* **2022**, *22*, 7034−7041.

(50) Jiang, W.; Yang, Z.; Li, Y.; Wang, G.; Jing, Q.; Guan, D.; Ma, J.; Zhang, W.; Qian, D. Spin-split valence bands of the ferromagnetic insulator $Cr_2Ge_2Te_6$ studied by angle-resolved photoemission spectroscopy. *J. Appl. Phys.* **2020**, *127*, No. 023901.

(51) Koroteev, Y. M.; Bihlmayer, G.; Gayone, J. E.; Chulkov, E. V.; Blügel, S.; Echenique, P. M.; Hofmann, P. Strong spin-orbit splitting on Bi surfaces. *Phys. Rev. Lett.* **2004**, *93*, No. 046403.